



HAL
open science

Simulations of weak-beam diffraction contrast images of dislocation loops by the many-beam Howie-Basinski equations

Zhongfu Zhou, Mike Jenkins, Sergei L Dudarev, Adrian Sutton, Mark Kirk

► **To cite this version:**

Zhongfu Zhou, Mike Jenkins, Sergei L Dudarev, Adrian Sutton, Mark Kirk. Simulations of weak-beam diffraction contrast images of dislocation loops by the many-beam Howie-Basinski equations. *Philosophical Magazine*, 2006, 86 (29-31), pp.4851-4881. 10.1080/14786430600615041 . hal-00513669

HAL Id: hal-00513669

<https://hal.science/hal-00513669>

Submitted on 1 Sep 2010

HAL is a multi-disciplinary open access archive for the deposit and dissemination of scientific research documents, whether they are published or not. The documents may come from teaching and research institutions in France or abroad, or from public or private research centers.

L'archive ouverte pluridisciplinaire **HAL**, est destinée au dépôt et à la diffusion de documents scientifiques de niveau recherche, publiés ou non, émanant des établissements d'enseignement et de recherche français ou étrangers, des laboratoires publics ou privés.



**Simulations of weak-beam diffraction
contrast images of dislocation loops by the many-beam
Howie-Basinski
equations**

Journal:	<i>Philosophical Magazine & Philosophical Magazine Letters</i>
Manuscript ID:	TPHM-05-Sep-0417.R2
Journal Selection:	Philosophical Magazine
Date Submitted by the Author:	24-Jan-2006
Complete List of Authors:	Zhou, Zhongfu; University of Oxford, Materials Jenkins, Mike; University of Oxford, Materials Dudarev, Sergei; UKAEA Fusion, Theory and Modelling Sutton, Adrian; Imperial College, Physics Kirk, Mark; Argonne national Laboratory, Materials
Keywords:	transmission electron microscopy, defect analysis, defect structures, dislocation structures, dislocations, electron diffraction, electron microscopy, radiation damage
Keywords (user supplied):	



Simulations of weak-beam diffraction contrast images of dislocation loops by the many-beam Howie-Basinski equations

Z Zhou¹, M L Jenkins¹, S L Dudarev², A P Sutton³ and M A Kirk⁴

¹ Department of Materials, University of Oxford, Parks Road, Oxford OX1 3PH, UK

² EURATOM/UKAEA Fusion Association, Culham Science Centre, Oxfordshire OX14 3DB, UK

³ Department of Physics, Imperial College, Exhibition Road, London SW7 2AZ, UK

⁴ Materials Science Division, Argonne National Laboratory, Argonne, IL60439, USA

A computer program has been developed to solve numerically the Howie-Basinski equations of electron diffraction theory, which avoid the so-called column approximation. In this paper we describe the basis of the numerical approach, and apply it to simulate images of small loops in copper under a variety of weak-beam imaging conditions. Simulations were carried out for faulted Frank loops of size 2 – 10 nm with systematic variations in imaging parameters (the loop orientation, the diffraction vector, the deviation parameter, the loop depth, the foil thickness and beam convergence). Comparisons are made with experiments in ion-irradiated copper. The simulated images were found to be in good qualitative agreement with experimental TEM micrographs. We are able to reach conclusions on the likely visibility of very small clusters, and we discuss the implications of the simulations for experimental measurements of loop number densities and sizes.

1. Introduction

Dislocation loops and other small point-defect clusters in crystals are usually investigated by using diffraction contrast images produced by conventional transmission electron microscopy. For defects larger than about 5 nm, a combination of dynamical two-beam imaging and image contrast simulations has proven very successful for determining defect morphologies, see e.g. Jenkins and Kirk (2001). It has been found experimentally however that the visibility of very small clusters of size < 5 nm is usually better under weak-beam diffraction conditions (see for example Jenkins, Kirk and Fukushima, 1999). Image simulations carried out under the same weak-beam conditions are necessary for a full analysis of such images. So far very few simulations of weak-beam images of small clusters have been reported. The method used previously for simulating images of larger clusters under dynamical conditions has been to solve the Howie-Whelan (Howie and Whelan, 1961) set of ordinary differential equations, usually in their two-beam form, or equivalent formulations of dynamical diffraction theory. These approaches make use of the so-called column approximation. Several authors have examined the effects of the column approximation on both strong-beam images and weak-beam images of line dislocations, and have generally concluded that these are likely to be small (Jouffrey and Taupin, 1967; Howie and Sworn, 1970). However, Lewis and Villagrana (1979) have made analytical and numerical studies of Takagi's equations (Takagi, 1962; Takagi 1969), and claim that the column approximation is likely to be unreliable in the simulation of weak-beam images of single point-defects (and by inference small point-defect clusters). They found that the main image detail is not where the column approximation would predict, but is shifted sideways; and that fringe structures should develop due to

interference of waves within the characteristic Takagi triangle, which are not predicted by the column approximation. If we are interested in exploring the fine details of weak-beam images of small clusters, the use of the column approximation may therefore be undesirable.

In this paper we describe a new numerical algorithm for the simulation of diffraction contrast images by solving numerically the Howie-Basinski equations (Howie and Basinski, 1968), which avoid the column approximation. The program based on this algorithm is capable of simulating rapidly and accurately diffraction contrast images of dislocation loops under both weak-beam and strong-beam diffraction conditions. We first describe the theoretical basis of our program (less complete descriptions have been given earlier in two conference papers, Zhou *et al.* 2003, 2004) and some details of its implementation and testing. We then apply the program to carry out a systematic investigation of the weak-beam contrast of Frank dislocation loops in copper, and draw conclusions on the implications for the interpretation of experimental images.

In our simulations we did not take into account the effect of electron energy losses. Kirk *et al.* (2002) showed that in the case where the thickness of the foil did not exceed 60 nm, energy filtering had relatively little effect on the quality of the images. On the other hand, in the case of thicker foils the use of energy filtering gave rise to much higher quality images (Jenkins *et al.*, 2003). Our simulations assume that the relevant experimental images were obtained using energy filtering.

2. Theoretical basis and numerical procedure

The Howie-Basinski equation set gives approximate solutions of the time-independent Schrödinger equation describing high-energy electrons propagating through a crystalline foil containing a defect such as a dislocation or a dislocation loop. The wave function $\psi(\mathbf{r})$ of the electrons is written as a sum over the diffracted beams $\phi_{\mathbf{g}}(\mathbf{r})$ in the Bloch-wave form

$$\psi(\mathbf{r}) = \sum_{\mathbf{g}} \phi_{\mathbf{g}}(\mathbf{r}) e^{2\pi i(\mathbf{k} + \mathbf{g} + \mathbf{s}_{\mathbf{g}}) \cdot \mathbf{r}} \quad (1)$$

Here \mathbf{k} is the wave-vector of the electrons incident on the thin foil, and $\mathbf{s}_{\mathbf{g}}$ is the deviation parameter (also called excitation error) for the beam with diffraction (or reciprocal lattice) vector \mathbf{g} . The direction of the vector $\mathbf{s}_{\mathbf{g}}$ is parallel to the zone axis \mathbf{z} . The crystal potential is evaluated using the deformable ion approximation

$$V(\mathbf{r}) = \sum_{\mathbf{g}} V_{\mathbf{g}} e^{2\pi i \mathbf{g} \cdot (\mathbf{r} - \mathbf{R}(\mathbf{r}))} = \sum_{\mathbf{g}} V_{\mathbf{g}} e^{-2\pi i \mathbf{g} \cdot \mathbf{R}(\mathbf{r})} e^{2\pi i \mathbf{g} \cdot \mathbf{r}} \quad (2)$$

where $\mathbf{R}(\mathbf{r})$ is the (continuous) field of atomic displacements around the defect. The deformable ion approximation fails near the edge of the dislocation loop if the field of displacements is calculated using elasticity. However, more accurate results obtained using lattice models (Dudarev, 2003; Hudson *et al.*, 2004) show that deformations remain smooth and continuous even in the core of small defects, and singularities present in solutions found using elasticity can be eliminated by introducing a small regularizing correction in the denominators of the relevant formulae. For example, the deformable ion approximation is probably applicable *everywhere* in a crystal containing *interstitial* defects and edge dislocation loops. Also, the finite size of the mesh used in numerical simulations makes it possible to avoid

encountering anomalously large values of matrix elements of the distortion field $\partial R_i/\partial x_j$. At the same time there are cases where the magnitude of strain evaluated using lattice models approaches 100%, and in this case the deformable ion approximation is not applicable.

By inserting the above expressions for $\psi(\mathbf{r})$ and $V(\mathbf{r})$ into the Schrödinger equation and neglecting the second order derivatives we obtain the Howie-Basinski equations of dynamical electron diffraction (Howie and Basinski, 1968):

$$(\mathbf{k} + \mathbf{g} + \mathbf{s}_{\mathbf{g}}) \cdot \nabla \phi_{\mathbf{g}} = -i\pi U_0 \phi_{\mathbf{g}} - i\pi \sum_{\mathbf{g}'} (1 - \delta_{\mathbf{g}\mathbf{g}'}) U_{\mathbf{g}-\mathbf{g}'} e^{2\pi i(\mathbf{g}'-\mathbf{g}) \cdot \mathbf{R}(\mathbf{r})} e^{2\pi i(\mathbf{s}_{\mathbf{g}'}-\mathbf{s}_{\mathbf{g}}) \cdot \mathbf{r}} \phi_{\mathbf{g}'} \quad (3)$$

where $U_{\mathbf{g}} = -(2m/h^2)V_{\mathbf{g}}$ and $h = 2\pi\hbar$ is Planck's constant, and where we used the condition of energy conservation $E = h^2k^2/2m = h^2|\mathbf{k} + \mathbf{g} + \mathbf{s}_{\mathbf{g}}|^2/2m$.

It is convenient computationally to apply a gauge transformation to equation set (3). The gauge transformation is as follows:

$$\phi_{\mathbf{g}}(\mathbf{r}) = \Phi_{\mathbf{g}}(\mathbf{r}) e^{-2\pi i \mathbf{g} \cdot \mathbf{R}(\mathbf{r})} e^{-2\pi i \mathbf{s}_{\mathbf{g}} \cdot \mathbf{r}} e^{-i\pi \frac{U_0}{(\mathbf{k}+\mathbf{g}+\mathbf{s}_{\mathbf{g}})_z} z} \quad (4)$$

The Howie-Basinski equations (3) become

$$\begin{aligned} (\mathbf{k} + \mathbf{g} + \mathbf{s}_{\mathbf{g}}) \cdot \nabla \Phi_{\mathbf{g}} &= 2\pi i (\mathbf{k} + \mathbf{g} + \mathbf{s}_{\mathbf{g}}) \cdot \mathbf{s}_{\mathbf{g}}^{(\mathbf{R})} \Phi_{\mathbf{g}} \\ &\quad - \pi i \sum_{\mathbf{g}'} (1 - \delta_{\mathbf{g}\mathbf{g}'}) U_{\mathbf{g}-\mathbf{g}'} e^{i\pi \frac{U_0}{(\mathbf{k}+\mathbf{g}+\mathbf{s}_{\mathbf{g}})_z} z - i\pi \frac{U_0}{(\mathbf{k}+\mathbf{g}'+\mathbf{s}_{\mathbf{g}'})_z} z} \Phi_{\mathbf{g}'} \end{aligned} \quad (5)$$

where $\mathbf{s}_{\mathbf{g}}^{(\mathbf{R})} = \mathbf{s}_{\mathbf{g}} + \nabla [\mathbf{g} \cdot \mathbf{R}(\mathbf{r})]$ is an effective local deviation parameter that varies spatially when the distortion field $\partial R_i/\partial x_j$, ($i, j = 1, 2, 3$) changes with position. Since $\phi_{\mathbf{g}}$ and $\Phi_{\mathbf{g}}$ in equation (4) differ only by a phase factor, the gauge transformation does not affect the intensities of the transmitted and diffracted beams. The argument of the phase factor in the right hand side of equation (5) may be expressed as

$$\frac{U_0 z}{(\mathbf{k} + \mathbf{g} + \mathbf{s}_{\mathbf{g}})_z} - \frac{U_0 z}{(\mathbf{k} + \mathbf{g}' + \mathbf{s}_{\mathbf{g}'})_z} \approx U_0 \frac{(s_{\mathbf{g}'} - s_{\mathbf{g}})z}{k^2} = \frac{V_0}{E} (s_{\mathbf{g}'} - s_{\mathbf{g}})z,$$

and is negligible in high energy electron diffraction. The distortion introduced by a defect appears only in the local deviation parameter $\mathbf{s}_{\mathbf{g}}^{(\mathbf{R})}$. If the crystal undergoes a homogeneous (affine) transformation then $\mathbf{s}_{\mathbf{g}}^{(\mathbf{R})}$ is a constant, and equation set (5) describes dynamical diffraction from a homogeneously deformed but otherwise perfect crystal. This observation suggests that equation set (5) may be solved numerically for an inhomogeneous (imperfect) crystal by dividing the crystal into small cells, where within each cell $\mathbf{s}_{\mathbf{g}}^{(\mathbf{R})}$ is taken as a constant.

Whereas the displacement field $\mathbf{R}(\mathbf{r})$ appears in the original Howie-Basinski equation set (3), it is the distortion field $\partial R_i/\partial x_j$ that appears in equation set (5). This is a principal benefit of the gauge transformation, equation (4). For example, the linear elastic strain field $(1/2)(\partial R_i/\partial x_j + \partial R_j/\partial x_i)$ decays more rapidly with distance from a defect than the displacement field itself. Perhaps more significantly the displacement field $\mathbf{R}(\mathbf{r})$ may not be a well-defined quantity because it depends on the choice of reference state. By contrast, the distortion field is independent of the choice of reference state for the displacement field.

This may be a particular advantage at an interface between two crystals where either perfect crystal may serve as a reference state to define $\mathbf{R}(\mathbf{r})$.

If the column approximation is applied to the transformed equations (5) we neglect the components of $\nabla\Phi_{\mathbf{g}}$ perpendicular to the zone axis z . Neglecting the phase factor we then obtain

$$\frac{\partial\Phi_{\mathbf{g}}}{\partial z} = 2\pi i s_{\mathbf{g}}^{(\mathbf{R})} \Phi_{\mathbf{g}} - \pi i \sum_{\mathbf{g}'} (1 - \delta_{\mathbf{g}\mathbf{g}'}) \frac{U_{\mathbf{g}-\mathbf{g}'}}{\beta_{\mathbf{g}}} \Phi_{\mathbf{g}'} \quad (6)$$

where $(\mathbf{k} + \mathbf{g} + \mathbf{s}_{\mathbf{g}}) \cdot \mathbf{s}_{\mathbf{g}}^{(\mathbf{R})}$ has been (well) approximated by $(\mathbf{k} + \mathbf{g} + \mathbf{s}_{\mathbf{g}})_z s_{\mathbf{g}}^{(\mathbf{R})}$, where $s_{\mathbf{g}}^{(\mathbf{R})}$ is the z -component of $\mathbf{s}_{\mathbf{g}}^{(\mathbf{R})}$ and $\beta_{\mathbf{g}} = (\mathbf{k} + \mathbf{g} + \mathbf{s}_{\mathbf{g}})_z$. Equation set (6) is equivalent to the Howie-Whelan equations (Howie and Whelan, 1961, Hirsch *et al.*, 1977). Thus, the essential point of the Howie-Basinski equations (as well as the Takagi equations derived earlier, Takagi, 1962) is that the diffracted beams propagate through the crystal along directions inclined to the zone axis, and by solving these equations one can avoid making the column approximation.

The accuracy of the Howie-Whelan equations can be improved by retaining the (x, y) -components of vector $\mathbf{s}_{\mathbf{g}}^{(\mathbf{R})}$. In this case we arrive at the *modified* Howie-Whelan equations

$$\frac{\partial\Phi_{\mathbf{g}}}{\partial z} = \frac{2\pi i}{\beta_{\mathbf{g}}} (\mathbf{k} + \mathbf{g} + \mathbf{s}_{\mathbf{g}}) \cdot \mathbf{s}_{\mathbf{g}}^{(\mathbf{R})} \Phi_{\mathbf{g}} - \pi i \sum_{\mathbf{g}'} (1 - \delta_{\mathbf{g}\mathbf{g}'}) \frac{U_{\mathbf{g}-\mathbf{g}'}}{\beta_{\mathbf{g}}} \Phi_{\mathbf{g}'}. \quad (7)$$

These equations take into account the full three-dimensional nature of lattice distortions $\partial R_i / \partial x_j$ but still make the column approximation.

Anomalous absorption is taken into account in the usual phenomenological way by introducing an absorptive potential (i.e. an imaginary part of the Fourier components of the potential) as given by Hashimoto *et al.* (1960), and Humphreys and Hirsch (1968). The complex Fourier components of the potential are calculated using the program originally given by Bird and King (1990) and modified by Dudarev *et al.* (1995).

In principle, the method described above is capable of simulating diffraction contrast images of any defect provided that its distortion field can be found. In the present paper we use linear, isotropic elasticity theory to obtain the distortion fields of dislocation loops using expressions derived from the displacement fields of angular dislocations given by Yoffe (1960). This method has previously been used by Saldin and Whelan (1979). For some materials such as copper or iron anisotropic elasticity is more accurate, but our aim in this paper is to explore systematic trends in weak-beam imaging of loops, for which isotropic elastic fields are adequate and computationally more expedient. In numerical image simulations the elastic field of a circular dislocation loop was approximated by the field of a 20-sided polygonal loop.

3. Numerical solution of the Howie-Basinski equations

The propagation of diffracted beams inclined to the zone axis z gives rise to a non-zero projection of the vector $(\mathbf{k} + \mathbf{g})$ onto the (x, y) plane, and we take this into account by a linear interpolation procedure. The crystal containing a defect is divided into thin slices normal to z and each slice is divided into small rectangular cells parallel to the x and y axes. The distortion field determining $\nabla[\mathbf{g} \cdot \mathbf{R}(\mathbf{r})]$ is approximated as a constant field throughout each cell. First, propagation of beams along the zone axis through each cell is

1
2
3
4 treated using the modified Howie-Whelan equations (7). To take account of the inclined
5 propagation of beams the amplitudes of beams on entry into each cell are equated to a linear
6 combination of amplitudes exiting from cells in the previous slice, with weights proportional
7 to the projections of the vector $(\mathbf{k} + \mathbf{g})$ on the x and y axes. The relevant cells of the
8 previous slice are the cell lying directly above, as in the column approximation, and one
9 or two adjacent cells along $-(\mathbf{k} + \mathbf{g} + \mathbf{s}_g)$. The term $s_g^{(\mathbf{R})}$ is evaluated for each cell of the
10 next slice, and equation set (7) is solved again. The process is repeated slice by slice to
11 find the beam amplitudes at the exit surface of the foil. In the Appendix we show that this
12 interpolation procedure yields an exact solution of the Howie-Basinski equations in the limit
13 of an infinitesimal cell size. In practice the numerical procedure uses a finite cell size which is
14 determined by the size and structure of the defect to be resolved, and also by requirements of
15 numerical convergence. For the loops considered in this work we find that cell sizes smaller
16 than 0.1 nm are required (Zhou *et al.* 2003).
17
18
19
20
21

22 4. Program tests and initial applications

23
24 Tests were carried out to confirm that our program reproduces established simulated and
25 experimental results.
26

- 27 • Calculations were made of thickness fringes of a perfect crystal in the two-beam ap-
28 proximation, which is a special case where the inclined propagation of diffracted beams
29 does not affect the observed intensities and where the Howie-Whelan equations can be
30 solved analytically. The numerical method and the analytical approach gave identical
31 results.
32
33
- 34 • Simulations were made of black-white (B-W) contrast images of dislocation loops under
35 two-beam dynamical conditions, and compared with simulated images available in the
36 literature for the same loop geometries. Again agreement is good (see Figure 1). This
37 is not a rigorous test of the ability of our program to simulate accurately weak-beam
38 images of such loops, since B-W images are sensitive to the long-range strain field of
39 the loop, whilst weak-beam images originate from regions of higher strain near the
40 dislocation cores. For B-W contrast images the use of the column approximation, and
41 even the two-beam approximation, are unlikely to cause problems. Nevertheless it was
42 a necessary condition that our program simulate such images successfully.
43
44
- 45 • Simulations were made of the weak-beam contrast of dislocation loops in silicon and
46 compared with experimental results (Zhou *et al.* 2004). Again, good agreement was
47 found. In particular the expected inside-outside contrast behaviour of inclined loops of
48 size greater than about 5 nm when imaged in $\pm\mathbf{g}$ was found, and this enables the loop
49 nature to be determined. Also, sections of flat-on loops with $\mathbf{g} \cdot \mathbf{b} = 0$ but $\mathbf{g} \cdot \mathbf{b} \times \mathbf{u} \neq 0$
50 were found to exhibit the weak double-peak contrast found experimentally (Zhou *et*
51 *al.* 2003). The sideways translation of images simulated without the use of the column
52 approximation noted by Lewis and Villagrana (1979) was confirmed. For loops in this
53 size range (> 5 nm) it is found experimentally that the contrast is not very sensitive
54 to small changes in diffraction conditions, and this was borne out by the simulations.
55 For smaller loops this is not the case. This is discussed in the following section.
56
57
58
59
60

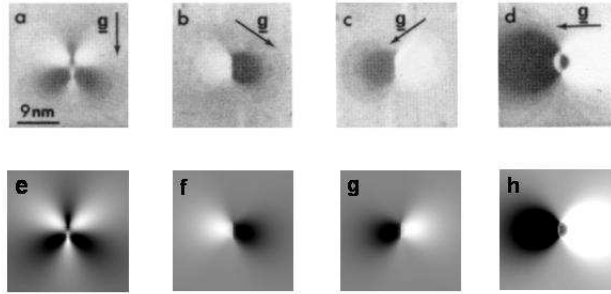


Figure 1: Simulated dark-field images of a perfect dislocation loop with $\mathbf{b} = 1/2[01\bar{1}]$ under two-beam dynamical conditions. The original images of Eyre *et al.* (1977) are shown above ((a) to (d)) and our images are shown below ((e)-(h)). (a) and (e) $\mathbf{g} = 200$, $\mathbf{g} \cdot \mathbf{b} = 0$; (b) and (f) $\mathbf{g} = 11\bar{1}$, $\mathbf{g} \cdot \mathbf{b} = 1$; (c) and (g) $\mathbf{g} = 1\bar{1}1$, $\mathbf{g} \cdot \mathbf{b} = 1$; (d) and (h) $\mathbf{g} = 022$, $\mathbf{g} \cdot \mathbf{b} = 2$. Loop diameter is ~ 5 nm. Foil thickness and loop depth are set according to Eyre *et al.* (1977).

5. Simulations of weak-beam images of Frank loops in copper

In this section we describe a systematic study of the contrast under weak-beam diffraction conditions of small Frank loops in copper. This choice was motivated by the availability of experimental images taken under well-controlled diffraction conditions of small point-defect clusters in ion-irradiated copper (Jenkins *et al.* 1999). These authors carried out a systematic study of the visibility and image size variations of defects in a (110) foil of thickness about 60 nm when imaged in $\mathbf{g} = \pm 002$. These defects had geometries based on Frank loops, although some were dissociated and complete stacking-fault tetrahedra were also present. For this foil orientation and diffraction vector all Frank loops have $|\mathbf{g} \cdot \mathbf{b}| = \frac{2}{3}$ and so according to the invisibility criterion should be in contrast. Two sets of Frank loops (those with $\mathbf{b} = \frac{1}{3}[1\bar{1}1]$ and $\frac{1}{3}[\bar{1}11]$) are edge-on, and two sets (with $\mathbf{b} = \frac{1}{3}[111]$ and $\mathbf{b} = \frac{1}{3}[11\bar{1}]$) lie on planes inclined at 35° to the beam direction. Jenkins *et al.* (1999) followed the contrast changes of individual clusters as a function of the sign of \mathbf{g} and the sign and magnitude of the deviation parameter $\mathbf{s}_{\mathbf{g}}$, with $|\mathbf{s}_{\mathbf{g}}|$ ranging from 0.15 nm^{-1} to 0.3 nm^{-1} . In the $(\mathbf{g}, n\mathbf{g})$ notation sometimes adopted to describe weak-beam imaging conditions (where the image is taken in the reflection \mathbf{g} and the Ewald sphere cuts the line of systematic reflections at $n\mathbf{g}$) n varies from ≈ 3.75 to 6.5 since the microscope was operated at 100 kV. The depths of these individual loops were measured using stereo microscopy.

The simulations we show below are for similar conditions as the experiments of Jenkins *et al.* (1999). We examine systematically the influence of the main experimental parameters on the contrast of small Frank loops in a size range from 2 – 10 nm. These parameters include the magnitude $|\mathbf{s}_{\mathbf{g}}|$ of the deviation parameter, the foil thickness and the depth of the defect in the foil, and the beam convergence. The distortion field of the loops was obtained using isotropic elasticity theory, for loops of approximately circular shape (in fact, 20-sided regular polygons) as outlined above. The use of elasticity theory is likely to be a good approximation for loops of sizes greater than about 2 nm, but less good for smaller loops (Zhou *et al.*, 2005) where molecular dynamics (in the form of conjugate gradient minimization of the potential

energy of a large system of interacting atoms) would have to be used to find displacement fields. This is the reason why here we restrict the simulations to loops of size ~ 2 nm or greater.

5.1. Qualitative evaluation of simulated images

5.1.1. The influence of the column approximation, dynamical effects and comparisons with experimental images

Figure 2 shows images of a 5 nm edge-on Frank loop simulated using (i) the full Howie-Basinski approach, including eight systematic reflection; (ii) as (i) but using the column approximation to solve the modified Howie-Whelan equations (7) rather than the Howie-Basinski equations; and (iii) as (ii) but in the two-beam approximation. In each case images are shown for three weak-beam conditions. Experimental images are shown for comparison. The computed images show subtle contrast changes but apart from the image shifts found in the Howie-Basinski approach (not shown explicitly in the figure) there is little to distinguish them and all seem reasonable matches to the experimental images. As shown in Figure 3, many-beam calculations suggest that complex image structures not directly related to the loop geometry may appear if higher-order reflections are satisfied ($n = 4, 5$ or 6 , in particular for $n = 5, 6$). These effects occur as a result of interference involving higher-order beams, and are absent in a 2-beam calculation. Such conditions where higher-order beams are excited are avoided experimentally. In our previous work (Zhou *et al.*, 2003, 2004) we showed that the effect of making the column approximation depends on the loop size, the diffraction condition and the geometrical relationship between the loop habit plane and the zone axis of diffraction. In general, the use of the full Howie-Basinski treatment is essential for very small loops (≤ 2 nm) that would appear as featureless white dots in weak-beam images. Figure 4 shows that the influence of the column approximation on weak-beam images is more serious for inclined loops than for edge-on loops.

5.1.2. Effect of tilting away from the [011] pole orientation

In practice weak-beam images are obtained by tilting along the Kikuchi band of the reflection of interest by several degrees, so that the specimen is oriented away from the exact [110] pole (zone axis) position. This is to avoid exciting non-systematic reflections which might have a perturbing effect on images. The so-called 'edge-on' loops will then not be exactly edge-on. The effect of this on images is shown in Figure 5 which compares images simulated at the [110] pole orientation and at the [560] orientation. In both cases only systematic reflections in the (002) row are included. It can be seen that the differences in the images are slight. For this reason most of the images shown below were computed for $\mathbf{z} = [110]$.

5.1.3. Effect of beam convergence

The effect of a finite beam convergence, here for beam semi-angles of 0.15° and 0.25° , is shown in Figure 6. The simulations were made by incoherently superimposing several images with differing angles of incidence. It can be seen that a beam convergence of this magnitude has little effect on the image. This is consistent with experiment. In a majority of the

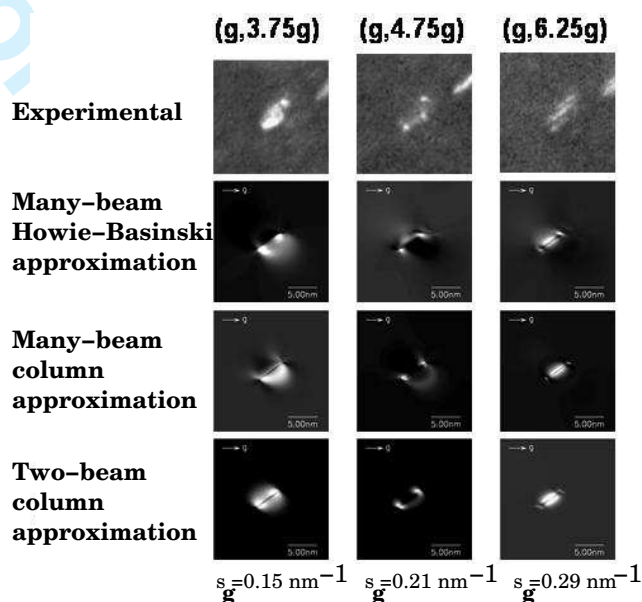


Figure 2: Simulated and experimental weak-beam images of edge-on loops in copper. The electron energy is 100 keV, and the beam direction is close to [110]. Images in each column are according to the deviation parameter labeled at the bottom of the column. Simulations were carried out using the many-beam approximation (including 8 beams, from 0 to 7g), where $\mathbf{g} = (002)$, with and without the column approximation, and the two-beam approximation. The loop diameter in the simulated images is 5 nm, foil thickness 60 nm, loop depth 30 nm and s_g is the deviation parameter.

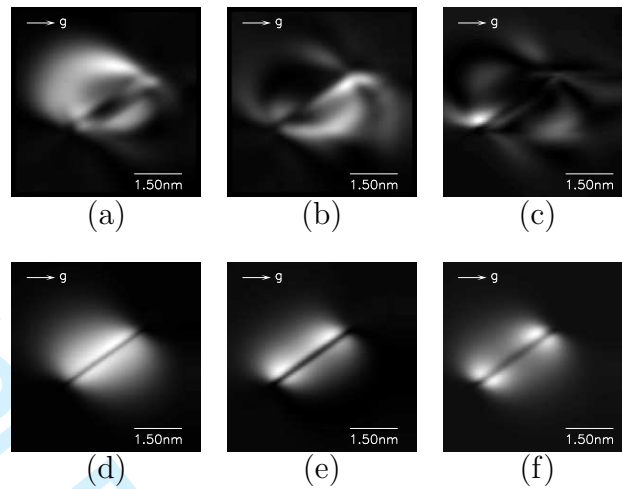


Figure 3: Simulated weak-beam images of an edge-on loop of diameter 3 nm in copper for $\mathbf{g} = 002$ at the $[110]$ pole. Foil thickness $t = 60$ nm. Loops are located around the centre of the foil. Weak-beam condition (a) & (d) ($\mathbf{g}, 4.0\mathbf{g}$), (b) & (e) ($\mathbf{g}, 5.0\mathbf{g}$), (c) & (f) ($\mathbf{g}, 6.0\mathbf{g}$); (a), (b) & (c) eight beams ($0\mathbf{g} - 7\mathbf{g}$) approximation; (d), (e) & (f) two-beam approximation for the same deviation parameters $|\mathbf{s}_{\mathbf{g}}|$. The many-beam calculations show that undesirable fine structure can occur if images are formed under dynamical diffraction conditions involving strong interference between several reflections belonging to a systematic row.

experiments carried out by Jenkins *et al.* (1999) the beam convergence semi-angle was set as 0.25° . Experimentally it was found that varying this angle in a range from 0.16° (a lower limit set by specimen drift during the long exposure time necessary in this case) and 0.32° (an upper limit set by the largest available condenser aperture) had a relatively small effect on images. There was only a weak tendency for measured defect sizes to decrease with decreasing beam convergence. We therefore take no further account of the finite beam convergence in the simulations reported below.

5.1.4. Effect of foil thickness

Figures 7 and 8 show sets of simulated images of edge-on and inclined Frank loops as a function of the foil thickness for loops ranging in size from 2 to 10 nm. In each case the depth of the loop in the foil and the deviation parameter remains the same. It can be seen that the images vary significantly with foil thickness, and that they do not always look like simple white dots. The images show the same periodic variation as the thickness fringes. At a foil thickness corresponding to a thickness-fringe minimum, the contrast is fairly strong and may show weak black-white features similar to those found for larger loops under dynamical two-beam imaging conditions. At a foil thickness corresponding to a thickness-fringe maximum the contrast is weak and smaller defects may effectively be invisible.

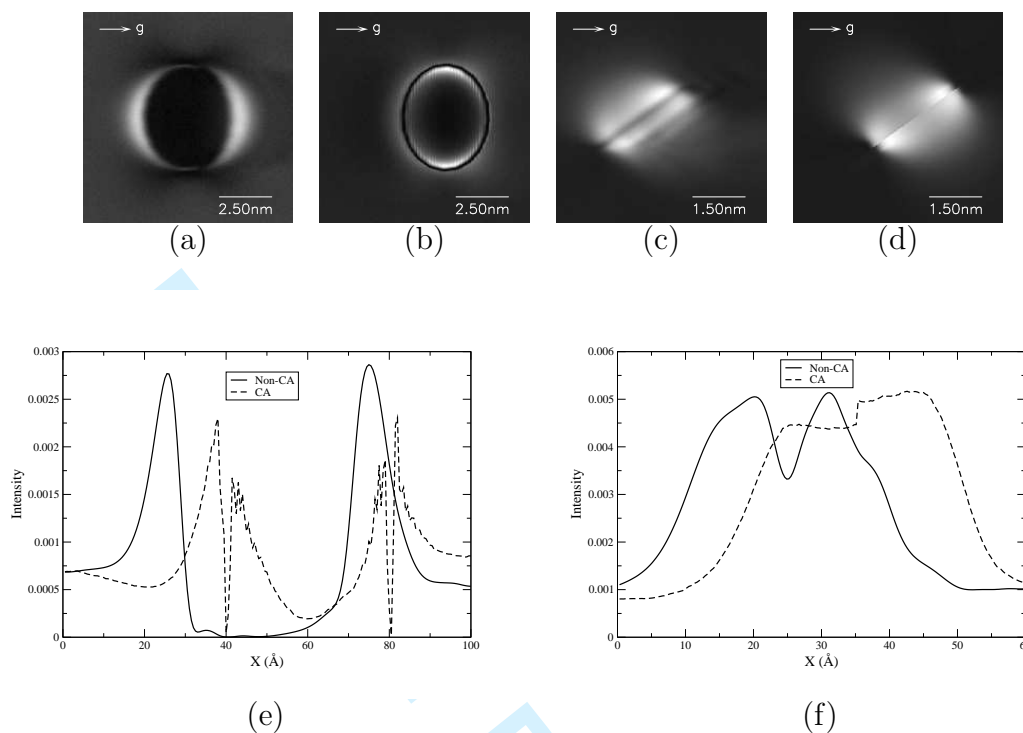


Figure 4: Simulated weak-beam images of inclined and edge-on vacancy loops in copper for $\mathbf{g} = 002$ at the $[110]$ pole. Foil thickness $t = 60$ nm and loops are located at the centre of the foil. The weak-beam condition is $(\mathbf{g}, 5.5\mathbf{g})$. (a) non-column approximation, (b) column approximation for an inclined loop of size 5 nm with $\mathbf{b} = 1/3[111]$; (c) non-column approximation, (d) column approximation (CA) for an edge-on loop of size 3 nm with $\mathbf{b} = 1/3[1\bar{1}1]$; (e) shows the intensity profile of the images cut through the center of (a) and (b) horizontally, and (f) shows the similar profiles for (c) and (d). In the simulations the stacking-fault contrast has been suppressed in order to emphasize more strongly the effect of the column approximation. Other simulations in the paper do include the stacking-fault contrast.

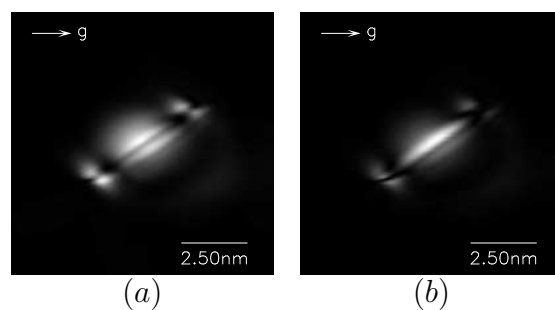
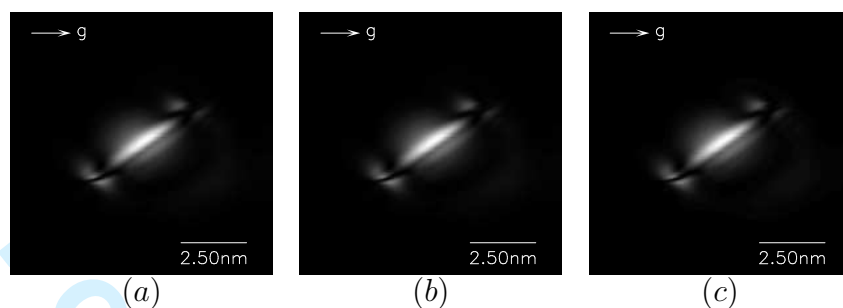
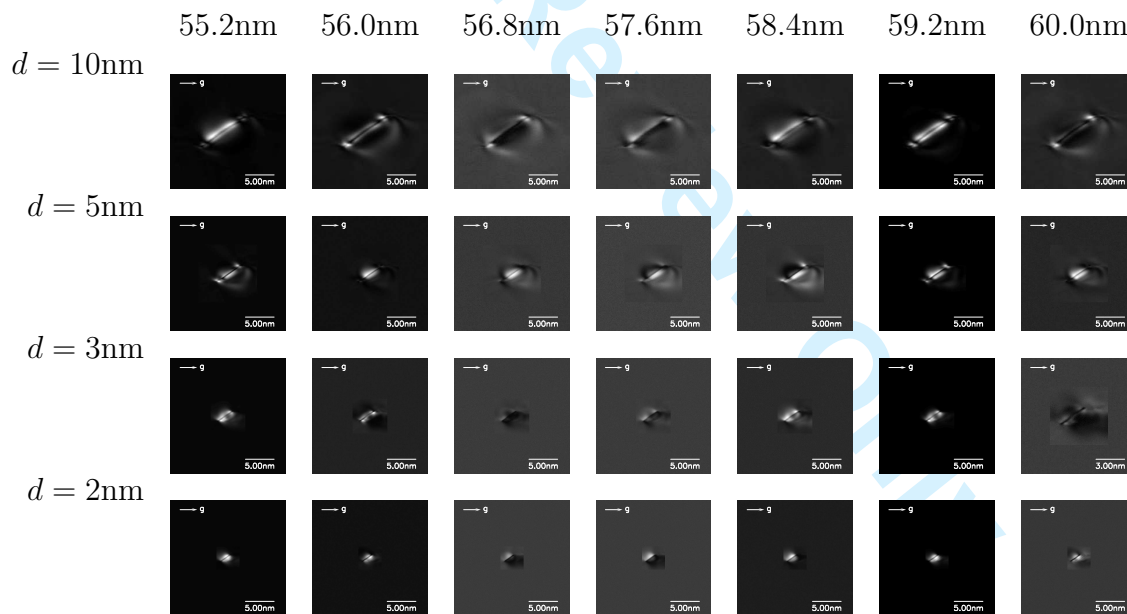


Figure 5: Simulated weak-beam images of an edge-on loop (a) along $[110]$ pole; (b) along $[560]$ pole. The weak-beam imaging condition is $(\mathbf{g}, 5.5\mathbf{g})$, where $\mathbf{g} = 002$, the diameter of the loop is 5 nm and the loop depth is 30 nm. The thickness of the foil is 60 nm.



19
20
21
22
23
24
25
26
27
28

Figure 6: Simulated weak-beam images of edge-on loop along the $[560]$ pole, (a) for an exactly parallel beam; (b) semi-angle of 0.15° ; (c) semi-angle of 0.25° . The weak-beam imaging condition is $(\mathbf{g}, 5.5\mathbf{g})$, where $\mathbf{g} = 002$, the diameter of the loop is 5 nm and the loop depth is 30 nm. The thickness of the foil is 60 nm.



51
52
53
54
55
56
57
58
59
60

Figure 7: Simulated weak-beam images of edge-on loops of diameter 10, 5, 3 and 2 nm with Burgers vector $\mathbf{b} = 1/3[1\bar{1}1]$. The images from left to right are according to the foil thickness given at the top of the columns. The thicknesses chosen span a range of one effective extinction distance. The loop depth is 30 nm and the diffraction condition is $(\mathbf{g}, 5.75\mathbf{g})$, where $\mathbf{g} = 002$. The background intensity varies according to the foil thickness.

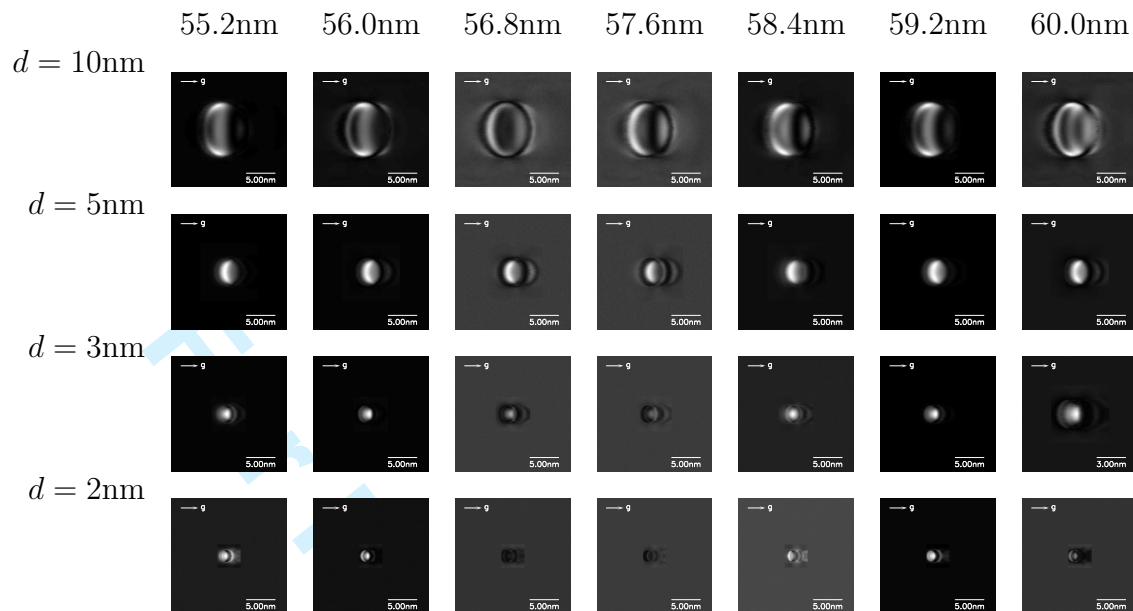


Figure 8: As Figure 7, for inclined loops with Burgers vector $\mathbf{b} = 1/3[11\bar{1}]$ and $\mathbf{g} = 002$.

5.1.5. Effect of loop depth

Figure 9 shows similar simulations for a range of depths of loops in the foil. The range of loop depths shown corresponds to the effective extinction distance $\xi_{\mathbf{g}}^{eff} \approx |\mathbf{s}_{\mathbf{g}}|^{-1}$. Loop depths of 10 and 14 nm correspond to a maximum of the weak-beam intensity for the operating reflection 002. The weak-beam images show considerable variation, changing both in appearance and in size.

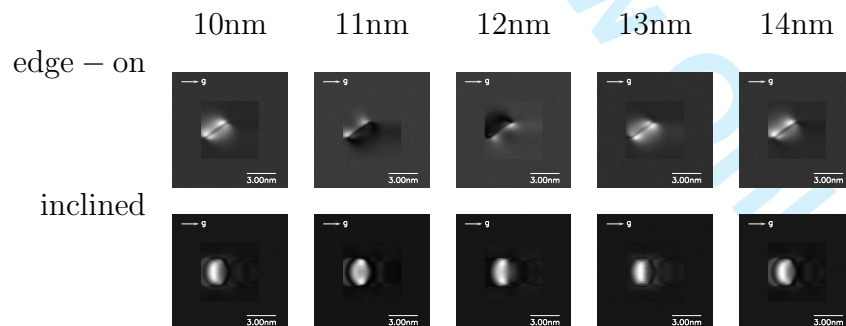
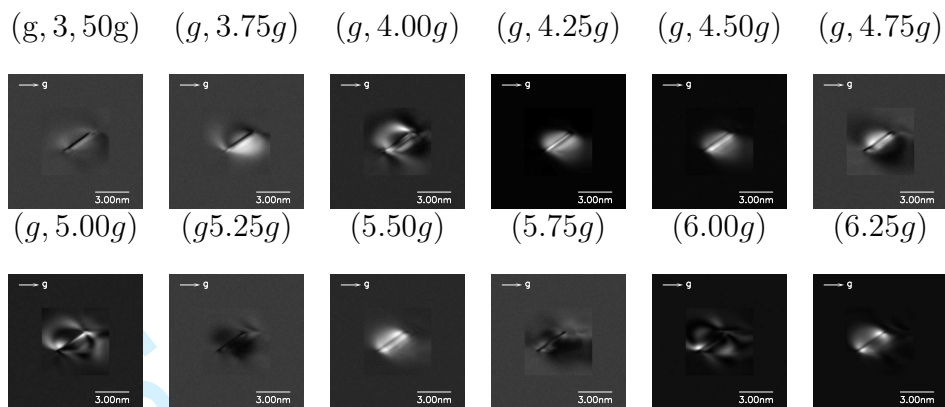


Figure 9: Simulated weak-beam images of edge-on and inclined loops of diameter 3 nm. The images from left to right are according to the depth of loops in the foil. Foil thickness is 60 nm and $\mathbf{g} = 002$.



18
19
20
21
22
23
24
25
26
27
28
29
30
31
32
33
34
35
36
37

Figure 10: Simulated weak-beam images of an edge-on loop of diameter 3 nm with Burgers vector $\mathbf{b} = 1/3[1\bar{1}1]$ for various weak-beam diffraction conditions from $(\mathbf{g}, 3.50\mathbf{g})$ to $(\mathbf{g}, 6.25\mathbf{g})$ with $\mathbf{g} = 002$. Foil thickness is 60 nm and the loop depth is 30 nm.

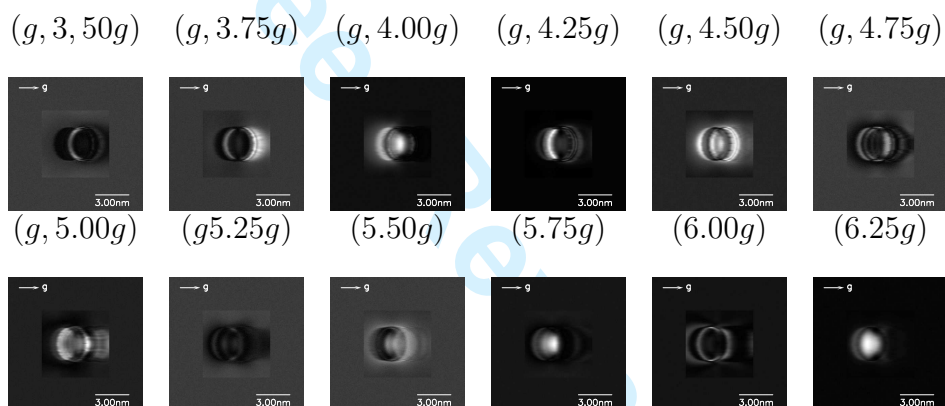


Figure 11: As Figure 10, for an inclined loop with Burgers vector $\mathbf{b} = 1/3[11\bar{1}]$ and for $\mathbf{g} = 002$.

5.1.6. Effect of deviation parameter

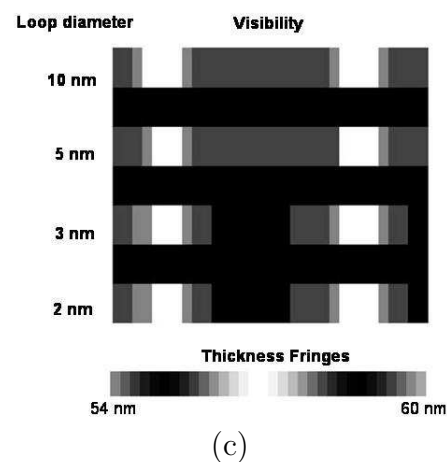
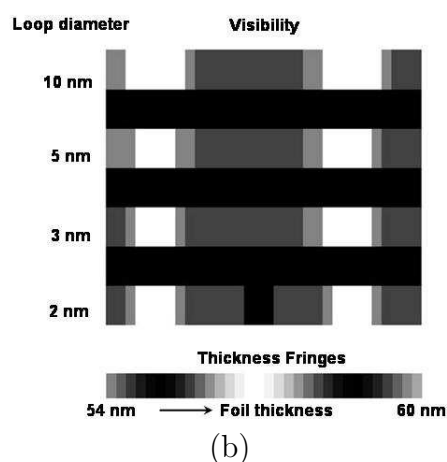
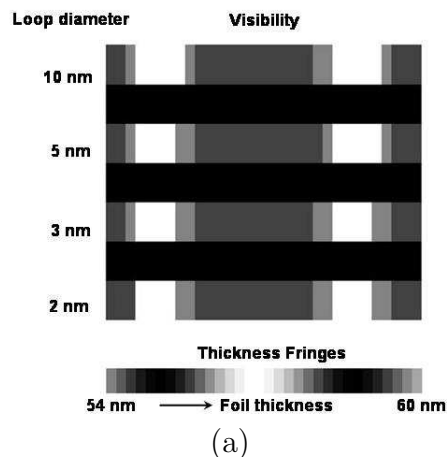
The effect of changes in deviation parameter $|\mathbf{s}_{\mathbf{g}}|$ are shown in Figures 10 and 11. The simulated images show marked differences in contrast for small differences in deviation parameter, as found experimentally. For integer values of n the contrast is substantially affected by the many-beam diffraction effects, as discussed in §5.1.1. It can be seen that this occurs for both edge-on and inclined loops. We have seen from Figures 7, 8 and 9 that contrast of a defect under weak-beam diffraction conditions depends strongly on its position relative to the thickness fringes. The fringes have a periodicity $\xi_{\mathbf{g}}^{eff} \approx 1/|\mathbf{s}_{\mathbf{g}}|$, which therefore changes with a change in deviation parameter. The sensitivity of the contrast to $|\mathbf{s}_{\mathbf{g}}|$ is therefore understandable.

5.2. Quantitative evaluation of the simulations

Care must be taken in analysing quantitatively a series of images such as those shown in Figures 7 - 11. Clearly the images as presented show a qualitative agreement with weak-beam images observed experimentally. In general very small loops are seen as white dots, which may, but more likely do not, show much fine structure. If such images are to be interpreted quantitatively, to try to measure loop sizes or to make conclusions about visibility, we have to define suitable criteria for making measurements. Experimental measurements on these kinds of images have generally been made rather crudely. For example, image sizes have often been measured with an eyepiece directly from the original negative, or more frequently, from an enlarged print. Defects are judged not to be visible if they cannot be made out against the background, which may itself show some structure. Clearly measurements made in this way may be rather subjective. In this paper we have adopted a more systematic approach to evaluating the visibility of defects and to measuring their sizes.

5.2.1. Defect visibility

Electron microscope film is a non-linear medium, and so the question of defect visibility is not trivial. Nevertheless, and somewhat arbitrarily based on a qualitative assessment of images by eye, we differentiate the contrast shown by loops into four categories according to the maximum image intensity relative to background, $v = I_{max}/I_{background}$. If $v < 3$ we consider visibility to be very low, such that the defect is effectively invisible. If $3 < v < 10$ we consider that visibility is low, but the defect is likely to be detected. For $10 < v < 20$ visibility is reasonably good, whereas for $v > 20$ the visibility is rated very good. Based on these categories, the visibilities of loops as functions of the experimental parameters are shown schematically in Figures 12 - 14. In each case the foil thickness varies along the x coordinate from 54 nm to 60 nm, within the range measured in the experiments and encompassing one thickness fringe cycle. The visibility of loops according to loop size is shown in Figure 12 for the following cases: (a) an edge-on loop; (b) an inclined loop in inside contrast and (c) an inclined loop in outside contrast. Generally loops of size 5 nm or more are always visible whatever their geometry, although their visibility may be low. Loops of size 3 nm or less may be effectively invisible for some foil thicknesses. The visibility of loops, especially very small loops, also depends on their geometry. The visibility is best for edge-on loops, and the visibility in inside-contrast is higher than in outside contrast. The visibility of a 3 nm loop as a function of loop depth is shown in Figures 13. In Figure 13(a) the loop depth is varied over the whole foil thickness in increments of 10 nm. In Figure 13(b) the depth is varied in smaller increments over a depth 27.5 nm to 31.0 nm, corresponding to one effective extinction distance. In both cases the dependence of the loop visibility on loop depth is weak, although the detailed appearance of the loop may change. Finally, in Figure 14 we show the loop visibility as a function of the deviation parameter $|\mathbf{s}_g|$. It can be seen that the visibility of a 3 nm loop depends sensitively on $|\mathbf{s}_g|$. Small variations in $|\mathbf{s}_g|$ change the loop visibility markedly. Again this is in accord with experiments.



52
53
54
55
56
57
58
59
60

Figure 12: Visibility of dislocation loops, with respect to loop size. (a) edge-on loops, (b) inclined loops in inside-contrast, (c) inclined loops in outside-contrast. In this and the following figures, very good visibility is shown white, reasonably good visibility light grey, low visibility dark grey and very low visibility black. From top to bottom the loop diameters are 10, 5, 3, 2 nm. The thickness fringes are shown below the bars for comparison. Diffraction condition is $(g, 5.5g)$, where $g = 002$ and loop depth is 30 nm.

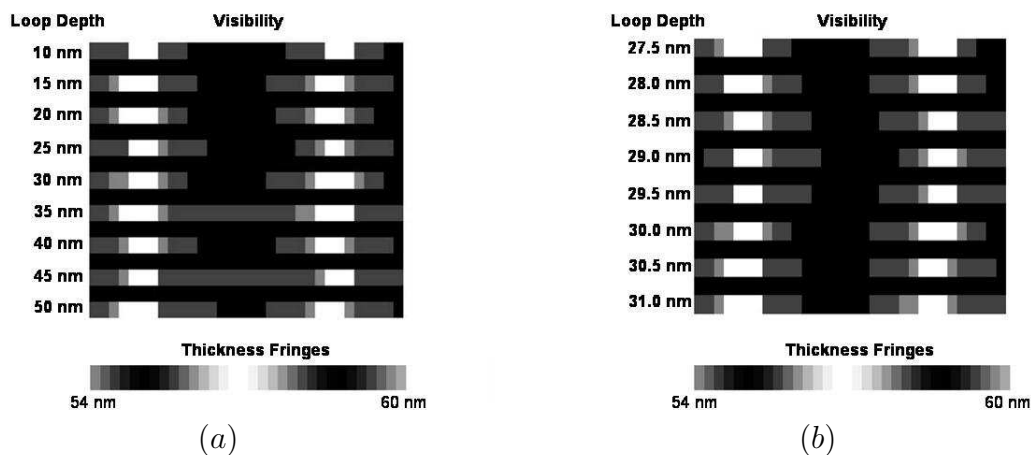


Figure 13: Visibility of a 3 nm inclined loop in outside-contrast with respect to loop depth. (a) from 10 nm to 50 nm with interval 5 nm; (b) from 27.5 nm to 31 nm within one effective extinction distance. The thickness fringes are shown below the bars for comparison.

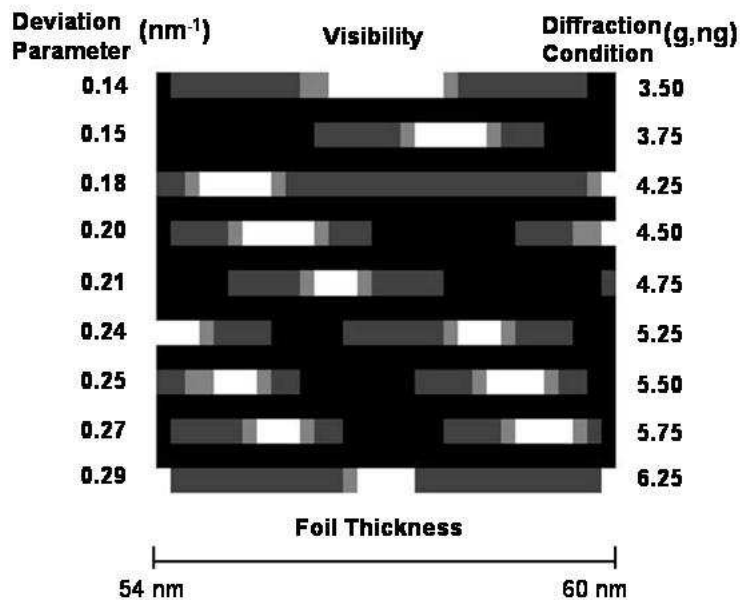


Figure 14: Visibility of inclined loops with respect to deviation parameter. From top to bottom the loop deviation parameter varies from 0.14 to 0.29 nm⁻¹. Loop diameter is 3 nm, loop depth 30 nm, and the foil thickness varies from 54 nm to 60 nm.

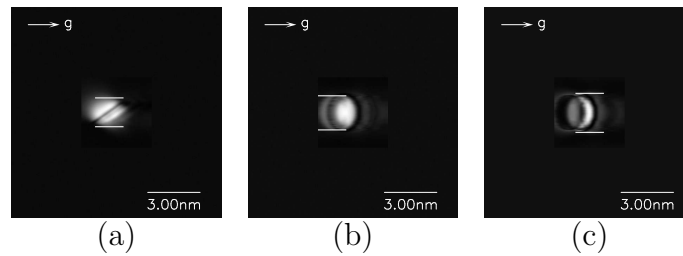


Figure 15: The simulated weak-beam images of (a) for edge-on dislocation loops, (b) for loops with inside-contrast, (c) for loops with outside-contrast. Diffraction condition is set to $(\mathbf{g}, 5.5\mathbf{g})$, where $\mathbf{g} = 002$. Foil thickness is 59 nm, and loop depth 30 nm. Bars for size measurements are labeled in the images. In (a) the vertical distance between the bars is divided by $\cos 32.56^\circ$ to obtain the size parallel to the loop habit plane. (c) represents a case when the size measurement made by the computer might overestimate the size measured by eye.

5.2.2. Defect sizes

The eye is sensitive to changes in contrast, and so some absolute contrast level may not be the best choice of the ‘edge’ of the contrast figure. The simulations shown in the figures above consist of a square 200×200 array of pixels with the diffraction vector \mathbf{g} running horizontally from left to right. We define the top edge of the contrast figure as follows. First, we examine the horizontal rows of pixels and identify the first pixel p where the contrast relative to background exceeds 15%. Then in the vertical column of pixels containing p we check if the change in contrast $(I_p - I_{p-1})/I_{p-1}$ exceeds some threshold value χ . If so pixel p defines the upper edge of the contrast figure. If not the process is repeated until a pixel p' is found which does satisfy the criteria. Good agreement with measurements made by eye were obtained by choosing $\chi = 0.04$ although this was decreased automatically if no two successive pixels showed a contrast change exceeding 0.04. A similar procedure was then repeated to locate the lower edge of the contrast figure. For inclined loops the loop size was then taken as the vertical difference between the two measurements. This corresponds to measuring the size of the loop in a direction perpendicular to \mathbf{g} , where the image size is likely to be a maximum. For edge-on loops a similar procedure was used, but a geometrical correction was made so that effectively the size was measured parallel to the habit plane, which again corresponds to the maximum image size. These criteria were found to give good agreement with measurements made by eye of the same simulated images. Some simulated images with measurements labels are shown in Figure 15. If in future experimental images are analysed more quantitatively - if for example image intensities are measured directly from images obtained with an image plate or CCD camera - these criteria may need to be reassessed. Image plates and CCD cameras have a more linear response than photographic films.

Figure 16 shows values of the relative difference in the image size determined by the method described above and the true size of the simulated loop. In Figure 16 it may be seen that the variation of the image sizes for both edge-on and inclined loops is relatively small ($\pm 20\%$). The images of edge-on loops tend to be a little larger than the true loop size at

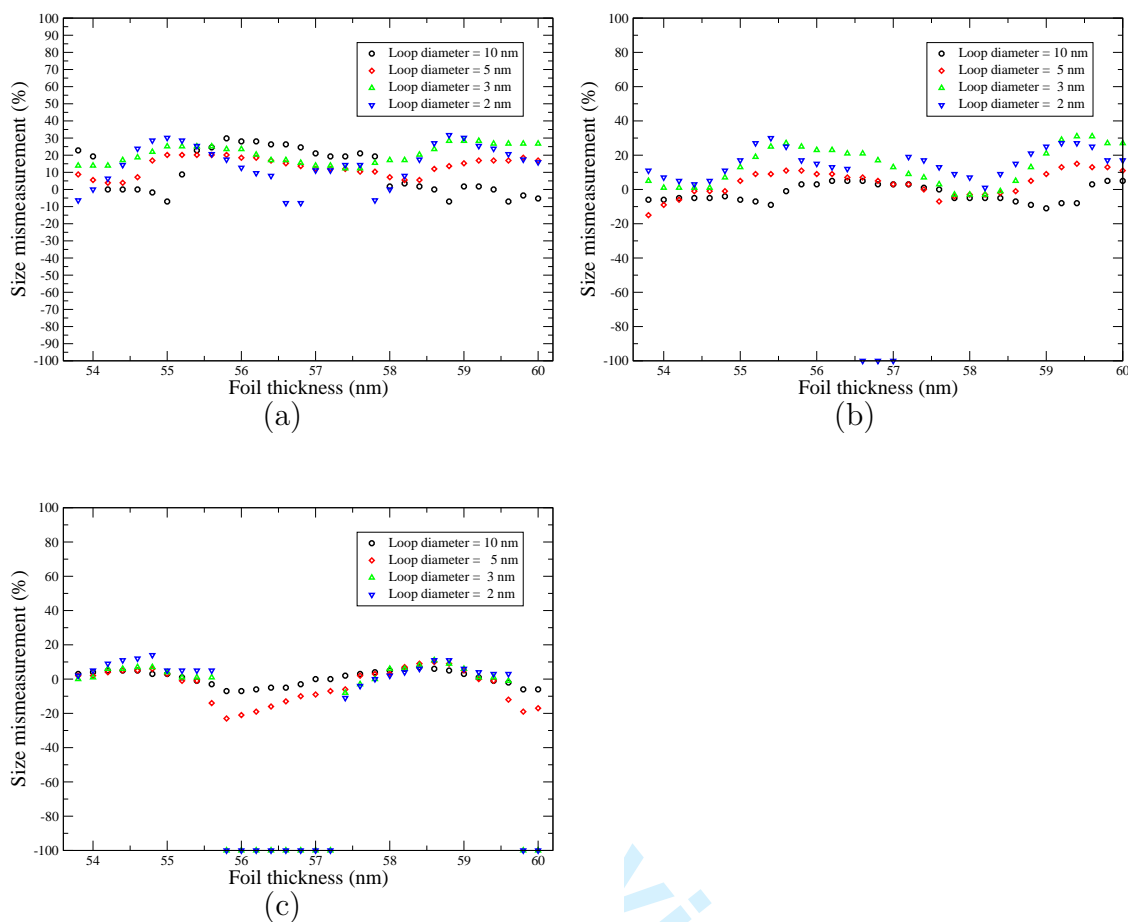


Figure 16: The difference between the sizes of simulated images, determined by the method described in the text, and the loop diameter of the simulation: (a) for edge-on loops; (b) for loops in inside-contrast; (c) for loops in outside-contrast. The data points at -100% indicate that for these conditions the loop was effectively invisible. The weak-beam condition is $(\mathbf{g}, 5.5\mathbf{g})$, where $\mathbf{g} = 002$.

small loop sizes, possibly as a consequence of the way we make the geometrical correction. For edge-on loops of size ≥ 5 nm on average there is a reasonably good correlation between the image size and the loop size for most foil thicknesses. For the inclined loops the image sizes are within $\pm 10\%$ of the true loop size, and there is little difference in measured loop size between inside and outside contrast (Figure 16 (b) and (c)).

The variation of the maximum image size with foil thickness for a 3nm loop situated at various depths D in the foil is shown in Figures 17 and 18. In all cases the image size is within about $\pm 20\%$ of the true loop size, and there is a periodic variation with foil thickness. Generally the image size is somewhat larger if the loop is located close to a thickness fringe minimum, where its visibility is high. The image size averaged over foil thickness is independent of loop depth and is close to the true loop size (Figure 18).

Finally the variation of the image size with the deviation parameter $|\mathbf{s}_{\mathbf{g}}|$ (or equivalently

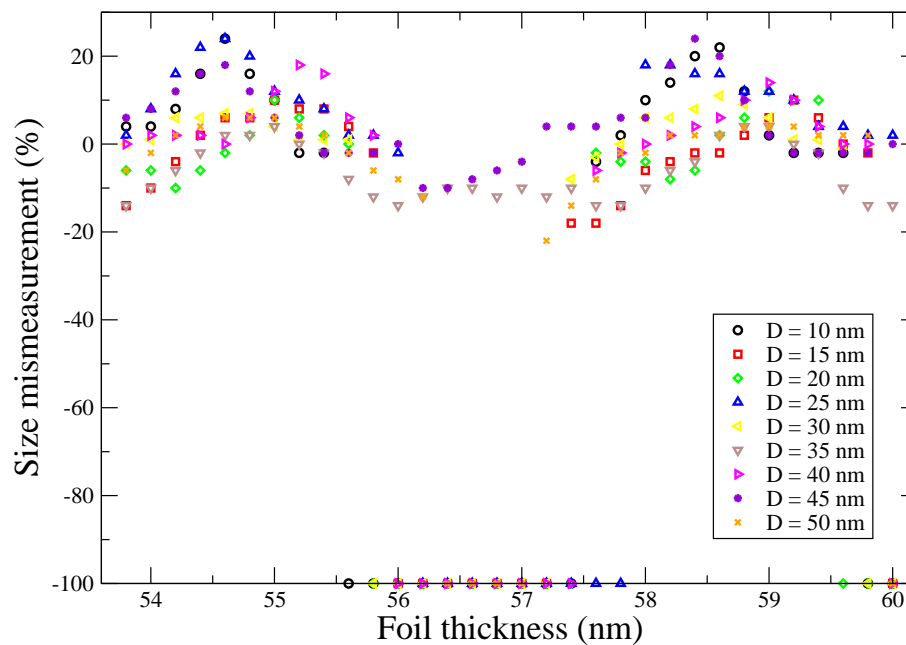


Figure 17: The difference between the measured size of weak-beam images and true loop size according the loop depth. Again the data points at -100% correspond to loops that are effectively invisible because of the very low contrast. Diffraction condition is set to $(\mathbf{g}, 5.5\mathbf{g})$, where $\mathbf{g} = 002$. D is the loop depth, the diameter of the loop is 3 nm.

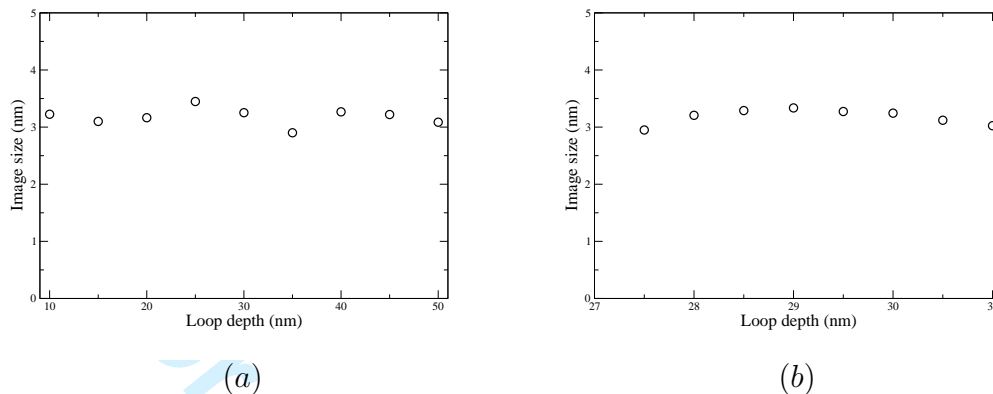


Figure 18: The variation of the image size of inclined dislocation loops as a function of the loop depth. Each value of size in the figure represents the average size of 32 images for foil thickness varying from 54 to 60 nm. The actual diameter of the loop is 3 nm. (a) for loops distributed with the depth from 10 nm to 50 nm throughout the file. (b) for loops located at different depths within one extinction distance. Diffraction condition is set to $(\mathbf{g}, 5.5\mathbf{g})$, where $\mathbf{g} = 002$.

the diffraction condition $n(\mathbf{g}, n\mathbf{g})$ for loops of size 2 nm and 3 nm is shown in Figure 19. Figure 19 (a) and (b) show simulated size measurements for individual loops of size 3 nm and 2 nm respectively. The foil thickness and loop depth for these simulations have been chosen arbitrarily within the range typical of the experiments. These simulated size measurements may be compared with the experimental size measurements shown in Figures 4 and 6 of Jenkins et al (1999). Part of their Figure 6 is reproduced for convenience in Figure 19 (e) and (f). These experimental size measurements pertain to two individual defects (labeled 17 and 12) which were produced in copper by heavy-ion irradiation at 20K. The size measurements were made at the irradiation temperature of 20K both before and after annealing the specimen to 120K. The aim of the experiment was to determine if the loops changed size on annealing. The image sizes for both the simulated images in (a) and (b) and the experimental images in (e) and (f) vary in a non-systematic way by about ± 1 nm, depending on $|\mathbf{s}_{\mathbf{g}}|$. The simulated results suggest it would be unwise to attempt to measure in experiments the sizes of individual loops to an accuracy of better than ± 1 nm in any single diffraction condition. Note however that if we average the simulated image size over foil thickness the sensitivity to $|\mathbf{s}_{\mathbf{g}}|$ is much less. This is shown in Figure 19 (c) and (d), which show averages over 32 images for foil thicknesses between 54 nm and 60 nm, encompassing one thickness fringe cycle. It may be seen that the average image size is close to the true loop size for all values of $|\mathbf{s}_{\mathbf{g}}|$. A consistent picture emerges that the measured size of a single defect, averaged over several diffraction conditions, corresponds to the true defect size. We can conclude therefore that the small change in average image size on annealing is probably significant and defects 17 and 12 have shrunk on annealing. The correspondence between the average image size and the true loop size is also important if we seek to measure

defect size *distributions*, as is discussed below.

6. Discussion

6.1. Image fine structure

Generally the simulated images of very small Frank loops show little fine structure (see Figures 7 and 8). However the simulated images of edge-on loops of size greater than about 3 nm do show fine structure consistent with experimental images (see Figure 2). This enables some experimental images to be identified as arising from particular Frank loop variants. Misinterpretation of such fine structure should be avoided: for example, an edge-on loop may give rise to a double-dot contrast (see the top right image in Figure 7) which might be misinterpreted as arising from two small adjacent loops. Such double-dot images are frequently seen in practice.

6.2. Implications for number density measurements

The simulations shown above have demonstrated that small Frank loops imaged using $\mathbf{g} = 002$ such that $\mathbf{g} \cdot \mathbf{b} \neq 0$ may nevertheless show only very weak contrast under some imaging conditions, and may effectively be invisible. A number of previous authors (see Jenkins and Kirk 2000 for a discussion) have recognised that very small clusters may have variable visibility when imaged under weak-beam diffraction conditions. Experimentally however it is known that defects are seen better under weak-beam conditions than any other imaging conditions. One possible solution to this difficulty, described by Jenkins *et al.* (1999) is to record several images of the same field of view differing only in diffraction condition, $|s_{\mathbf{g}}|$. By comparing several such images defects which are not visible in one micrograph may be picked up on another, so allowing all defects of size greater than the resolution limit to be counted. Figure 14 confirms that this approach is likely to be effective. The number of micrographs needed to be sure of detecting all resolvable defects depends on whether those loops having low visibility ($3 < \nu < 10$) are seen in practice, which will depend on factors such as the foil surface quality. In extreme cases as many as 6-8 micrographs may be required.

This technique however is very cumbersome and time consuming. Figure 12 suggests that most loops of size 5 nm or higher will show some contrast and that the proportion of Frank loops of size 3 nm or smaller which are likely not to be visible is of the order of 10-30%. This conclusion is compatible with the experiments and may be used as the basis of a rough correction to measured number densities.

Note that the above remarks apply to Frank loops which should be visible according to the conventional contrast criterion $\mathbf{g} \cdot \mathbf{b} \neq 0$. If other diffraction vectors are employed, or if dislocation loops of other types are present, the possibility that some loop variants have $\mathbf{g} \cdot \mathbf{b} = 0$ has to be considered. Such loops are likely to be invisible under weak-beam imaging conditions, necessitating a further systematic correction to number density measurements. Also, the possibility that in some materials perfect loops may slip out of the foil under the influence of surface image forces must be considered. For a discussion of these and other problems of loop counting, see chapter 5 of Jenkins and Kirk (2001).

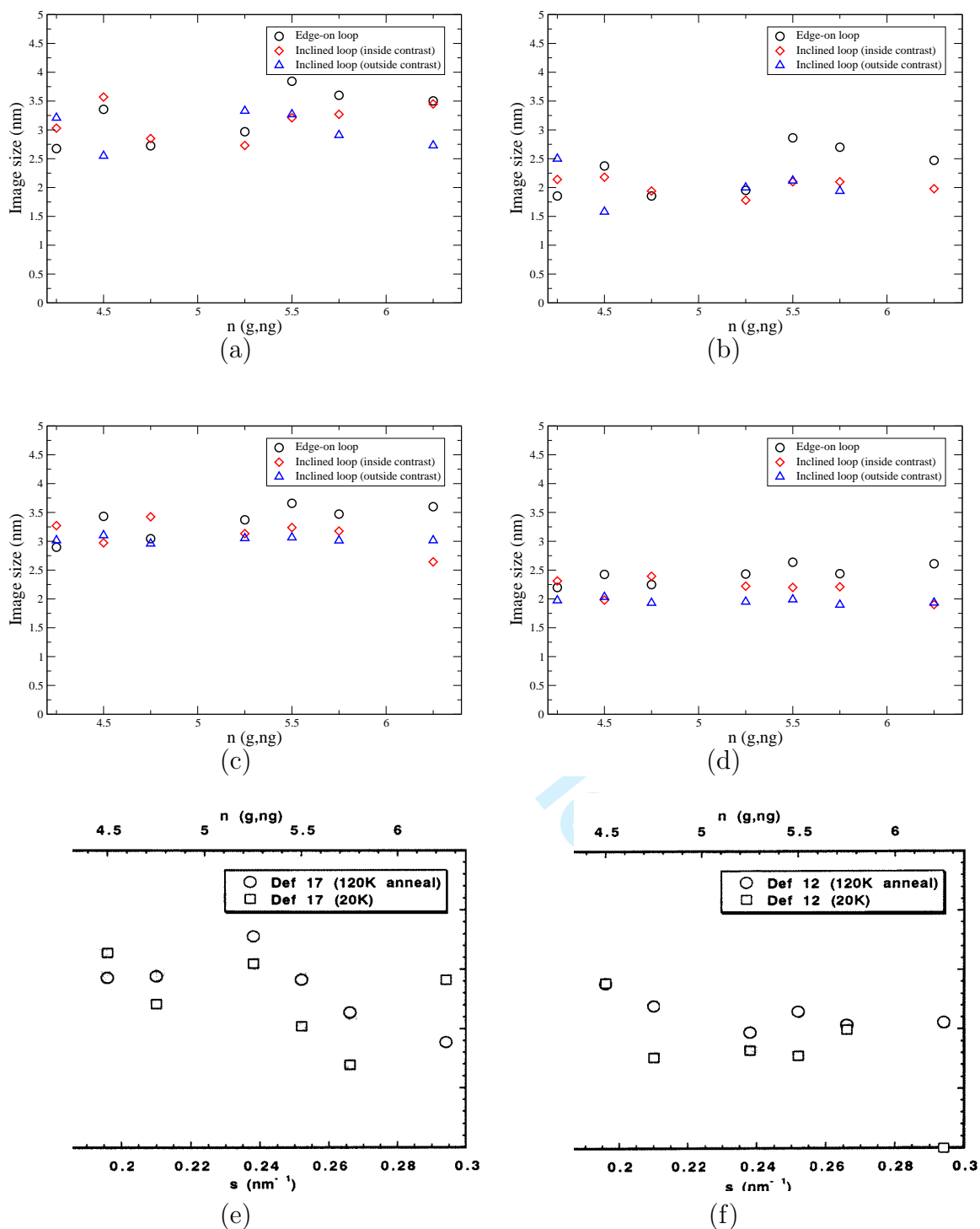


Figure 19: The image size measured from simulated and experimental images of dislocation loops under different weak-beam conditions. (a) and (b) are size measurements from simulated images for loops of diameter 3 nm and 2 nm separately, foil depth is around 59 nm; (c) and (d) are same measurements, but each value of the size measured is the average of 32 images for foil thickness from 54 to 60 nm in the simulations; (e) and (f) are experimental results for two defects (labeled 17 and 12) before and after annealing from 20 K to 120 K, and are from Figure 6 in Jenkins *et al.* (1999).

6.3. Implications for image size measurements

It is clear from the above that the weak-beam contrast of very small (~ 2 nm) clusters is sensitive to the exact imaging conditions. In most cases however the calculations presented in Figures 19-22 show the image sizes of Frank loops lie within about 20% of the true loop size. Sometimes the image size is larger than the true loop size, and sometimes smaller. These excursions occur about equally in both directions for inclined loops, whilst the image sizes of edge-on loops tend to be somewhat larger than the true loop size. The image size relative to the true loop size varies with loop morphology, loop depth, foil thickness and deviation parameter, but there seems to be no systematic trend with loop size. Both larger (10 nm) and smaller (2 nm) loops may appear larger or smaller than their true size, according to the imaging parameters. In general it is not practicable to determine the morphologies of individual loops, nor can their depth in the foil or the foil thickness be measured very accurately. It is therefore not possible to measure accurately the sizes of individual defects without carrying out the sort of detailed experiments described by Jenkins *et al.* (1999), where images of the same defect were obtained with systematic variations of $|s_{\mathbf{g}}|$. The simulations suggest that the true sizes of individual Frank loops can be measured to an accuracy of about ± 1 nm by determining the average maximum image size in a series of micrographs taken with different deviation parameters. Further simulations of images of defects of different morphologies are in progress to confirm this more generally.

Defect size distributions are often made in practice by measuring image sizes on a single micrograph. The simulations show that size distributions measured in this way are unlikely to be good representations of the true defect size distribution. The image size of a Frank loop of given size may differ from the true loop size by $\pm 20\%$, resulting in a broadening of the image size distribution relative to the true loop size distribution. Since however the image size is about equally likely to be smaller or larger than the true loop size, the average image size of the population is likely to be a reasonably good approximation to the average true loop size of the population.

7. Conclusions

- A computer program has been developed for solving the Howie-Basinski equations numerically. This program avoids the column approximation, and so is suitable for simulating weak-beam images of small point-defect clusters.
- Systematic simulations have been made of weak-beam images of small Frank loops in copper. These simulations show that the images of individual defects are sensitive to the values of the foil thickness, the defect depth and the deviation parameter. This is in agreement with experiment.
- The implications for measuring loop number densities and loop sizes have been discussed. Measurements of either of these quantities from single micrographs are liable to error and should be avoided if possible. Errors can be reduced by the analysis of several images of the same field of view taken with different deviation parameters $|s_{\mathbf{g}}|$.

- Further simulations for different defect types (e.g, stacking-fault tetrahedra) and diffraction geometries are in progress.
- Whilst we consider that the demonstrated variations with imaging parameters are important, the usefulness of these simulations to experiments is so far rather limited. The main reason is a need to evaluate the fine structure, visibility and sizes of images in the presence of random noise variations in the background, which are present in all experimental weak-beam images.

Acknowledgements

We are grateful to Professors P. B. Hirsch, D. J. H. Cockayne, C. B. Carter and R. Schäublin for stimulating discussions. Zhongfu Zhou is grateful to the EURATOM/UKAEA Fusion Association for the provision of a studentship. He is also grateful to St Hugh's College, Oxford, for the award of a Wei Lun Scholarship. Work at UKAEA was funded by the UK Engineering and Physical Sciences Research Council (EPSRC), by the EXTREMAT integrated project and by EURATOM.

References

- Bird, D. M. and King, Q. A., 1990, *Acta Cryst.* **A46**, 202
- Dudarev, S. L., Peng, L. M. and Whelan, M. J., 1995, *Surf. Sci.* **330**, 86.
- Dudarev, S. L., 2003, *Philos. Mag.* **83**, 3577
- Eyre, B. L., Mayer, D. M. and Perrin, R.C., 1977, *Journ. Phys. F: Metal Phys.* **7**, 1370.
- Hashimoto, H., Howie, A. and Whelan, M. J., 1960, *Philos. Mag.* **5**, 967.
- Hirsch, P.B., Howie, A., Nicholson, R., Pashley, D. W. and Whelan, M. J., 1977, *Electron Microscopy of Thin Crystals* (Krieger Publishing Company, Malabar, Florida)
- Howie, A. and Basinski, Z. S., 1968, *Philos. Mag.* **17**, 1039.
- Howie, A. and Sworn, H., 1970, *Philos. Mag.* **21**, 861.
- Howie, A. and Whelan, M. J., 1961, *Proc. Roy. Soc. London Ser. A* **263**, 217.
- Hudson, T. S., Dudarev, S. L. and Sutton, A. P., 2004, *Proc. Roy. Soc. London Ser. A* **460**, 2457
- Humphreys, C. J. and Hirsch, P. B., 1968, *Philos. Mag.* **18**, 115.
- Jenkins, M. L., Kirk, M. A. and Fukushima, H., 1999, *J. Electron Microscopy* **48**, 323.
- Jenkins, M. L. and Kirk, M. A., 2001, *Characterisation of Radiation Damage by Transmission Electron Microscopy*, Institute of Physics Series in Microscopy in Materials Science (Series Editors B. Cantor and M. J. Goringe)
- Jenkins, M. L., Martin, S. P., Hetherington, C. J. D., and Kirk, M. A., 2003, in: *Electron Microscopy: Its Role in Materials Science*, ed. J. R. Weertman, M. Fine, K. Faber, W. King and P. Liaw (The Minerals, Metals and Materials Society), p. 13.
- Jouffrey, B. and Taupin, D., 1967, *Philos. Mag.* **16**, 703.
- Kirk, M. A., Jenkins, M. L. and Fukushima, H., 2000, *Journ. Nucl. Mat.* **276**, 50.
- Kirk, M. A., Tweston R., Martin S. P., Hetherington C. J. D. and Jenkins M. L., 2002, *Microscopy and Microanalysis* **8**, suppl. 2, 622CD
- Lewis, A. L. and Villagrana, R. E., 1979, *Acta Cryst.* **A35**, 276.

René-Rasmussen, D. and Carter, C. B., 1991, Journ. Electron Microscopy Techniques **18**, 429.

Saldin, D. K. and Whelan, M. J., 1979, Phil. Trans. Roy. Soc. London **A292** 513.

Takagi, S., 1962, Acta Cryst. **15**, 1311

Takagi, S., 1969, Journ. Phys. Soc. Japan **26**, 1239

Yoffe, E. H., 1960, Philos. Mag. **5**, 161.

Zhou, Z., Dudarev, S. L., Jenkins, M. L. and Sutton, A. P., 2003, Proceedings of Electron Microscopy and Analysis Group Conference (Oxford), Inst. Physics Conf. Ser. **179**, 203.

Zhou, Z., Dudarev, S. L., Jenkins, M. L., Sutton, A. P. and Kirk, M. A., 2004, Mat. Res. Soc. Symp. Proc. **792**, page 491.

Zhou, Z., Dudarev, S. L., Jenkins, M. L., Sutton, A. P. and Kirk, M. A., 2005, Journ. Mater. Science and Engineering, in press.

Appendix: The Validity of the Interpolation Procedure

Here we show that a solution obtained using the interpolation procedure outlined in Section 3 is an exact solution of the Howie-Basinski equations (5) in the limit of an infinitesimal cell size. To illustrate the numerical solution we consider a weak-beam condition in which \mathbf{g} is selected from a systematic row of reflections $\mathbf{g}' = \mathbf{g}, 2\mathbf{g}, 3\mathbf{g}, \dots, n\mathbf{g}$, where n is an integer. We choose the x -axis to be parallel to the systematic row of \mathbf{g}' -vectors. The amplitudes of diffracted beams in this case are independent of coordinate y and the diffraction problem is two-dimensional.

Our approach is to use the modified Howie-Whelan equations (7) to propagate the diffracted beams along the zone axis, and to take account of the inclined propagation by equating beam amplitudes entering a slice normal the zone axis to linear combinations of beam amplitudes exiting adjacent cells in the previous slice. Let $\Phi_{g'}^{(in)}(\nu, z)$ and $\Phi_{g'}^{(out)}(\nu, z + \Delta z)$ denote the amplitudes of the diffracted beam $\mathbf{k} + \mathbf{g}'$ entering and exiting the ν 'th cell of the slice at z of thickness Δz . Within each slice there are rows of cells along the x -axis and ν increases along each row and from one row to the next along the y -axis. Let θ'_g denote the angle between the diffracted beam $\mathbf{k} + \mathbf{g}'$ and the zone axis (see Figure 20). The angle θ'_g is in the (x, z) plane, and

$$\tan \theta_{g'} = \frac{(\mathbf{k} + \mathbf{g}')_x}{(\mathbf{k} + \mathbf{g}')_z} \approx \frac{(\mathbf{k} + \mathbf{g}')_x}{(\mathbf{k} + \mathbf{g}' + \mathbf{s}'_g)_z}, \quad (8)$$

since $(\mathbf{s}'_g)_z \ll (\mathbf{k} + \mathbf{g}')_z$.

In the column approximation the amplitude $\Phi_{g'}^{(out)}(\nu, z + \Delta z)$ exiting the ν 'th cell of a given slice equals the amplitude $\Phi_{g'}^{(in)}(\nu, z + \Delta z)$ entering the ν 'th cell of the next slice. But for the inclined propagation considered here the amplitude entering the ν 'th cell of the next slice is set equal to a weighted average of the amplitudes exiting the cell directly above and an adjacent cell:

$$\Phi_{g'}^{(in)}(\nu, z + \Delta z) = \left(1 - \frac{\Delta z}{W} \tan \theta_{g'}\right) \Phi_{g'}^{(out)}(\nu, z + \Delta z) + \left(\frac{\Delta z}{W} \tan \theta_{g'}\right) \Phi_{g'}^{(out)}(\nu - 1, z + \Delta z), \quad (9)$$

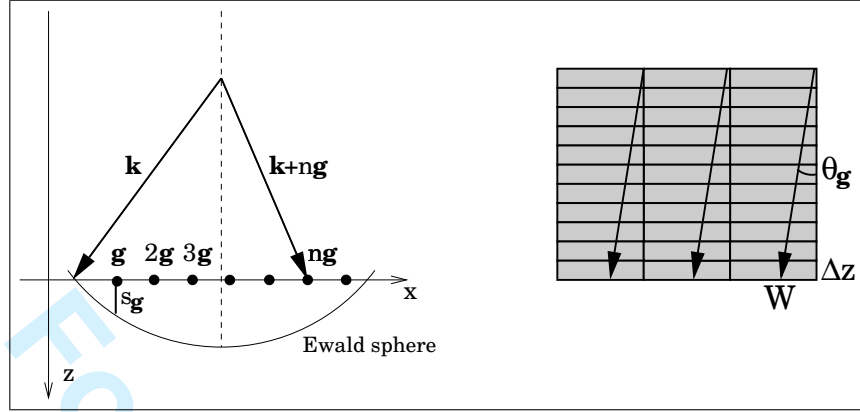


Figure 20: Schematic diagram to illustrate the geometry of the assumed diffraction conditions. The vertical broken line represents the zone axis, \mathbf{g} is a reciprocal lattice vector and \mathbf{k} is the wave vector of the incident beam of electrons. The geometry of diffraction illustrated in this figure corresponds to a weak-beam condition typically used in electron microscope imaging where the Ewald sphere *does not* pass through a reciprocal lattice point.

if $\theta_{g'}$ is positive and

$$\Phi_{g'}^{(in)}(\nu, z + \Delta z) = \left(1 + \frac{\Delta z}{W} \tan \theta_{g'}\right) \Phi_{g'}^{(out)}(\nu, z + \Delta z) - \left(\frac{\Delta z}{W} \tan \theta_{g'}\right) \Phi_{g'}^{(out)}(\nu + 1, z + \Delta z), \quad (10)$$

if $\theta_{g'}$ is negative. Here W is the length of a cell along x . The geometry is illustrated in Figure 20. The slices are assumed to be sufficiently thin for all the reflections \mathbf{g}' that $|(\Delta z/W) \tan \theta_{g'}| \ll 1$.

We now show the equivalence between the interpolation method and the original set of differential equations (5). We write the derivative $\partial\Phi_{g'}/\partial z$ as

$$\frac{\partial\Phi_{g'}(x, z)}{\partial z} = \lim_{\Delta z \rightarrow 0} \frac{\Phi_{g'}^{(in)}(x, z + \Delta z) - \Phi_{g'}^{(in)}(x, z)}{\Delta z}, \quad (11)$$

where the point x is located within the ν 'th cell. The calculation of $\Phi_{g'}^{(in)}(x, z + \Delta z)$ involves two steps. First, starting from the amplitude $\Phi_{g'}^{(in)}(x, z)$ incident on a given slice and integrating equations (7), we find the amplitude $\Phi_{g'}^{(out)}(x, z + \Delta z)$ of the wave coming out of the slice. Second, by using the interpolation formulae (9) and (10) we find the amplitude $\Phi_{g'}^{(in)}(x, z + \Delta z)$ of the wave incident on the next slice.

Substituting equation (9) into equation (11), we find that

$$\begin{aligned} \frac{\partial\Phi_{g'}(\nu, z)}{\partial z} &= \lim_{\Delta z \rightarrow 0} \frac{1}{\Delta z} \left\{ \left(1 - \frac{\Delta z}{W} \tan \theta_{g'}\right) \Phi_{g'}^{(out)}(\nu, z + \Delta z) \right. \\ &+ \left. \left(\frac{\Delta z}{W} \tan \theta_{g'}\right) \Phi_{g'}^{(out)}(\nu - 1, z + \Delta z) - \Phi_{g'}^{(in)}(\nu, z) \right\} \\ &= \lim_{\Delta z \rightarrow 0} \frac{1}{\Delta z} \left\{ \Phi_{g'}^{(out)}(\nu, z + \Delta z) - \Phi_{g'}^{(in)}(\nu, z) \right\} \end{aligned}$$

$$- \left(\frac{\Delta z}{W} \tan \theta_{g'} \right) \left[\Phi_{g'}^{(out)}(\nu, z + \Delta z) - \Phi_{g'}^{(out)}(\nu - 1, z + \Delta z) \right] \}. \quad (12)$$

The difference

$$\lim_{\Delta z \rightarrow 0} \frac{1}{\Delta z} \left\{ \Phi_{g'}^{(out)}(\nu, z + \Delta z) - \Phi_{g'}^{(in)}(\nu, z) \right\}$$

describes the effect of propagation of electrons through a slice in the direction of the zone axis and is given by the modified Howie-Whelan equations (7)

$$\lim_{\Delta z \rightarrow 0} \frac{1}{\Delta z} \left\{ \Phi_{g'}^{(out)}(\nu, z + \Delta z) - \Phi_{g'}^{(in)}(\nu, z) \right\} = \frac{2\pi i}{\beta_{\mathbf{g}}} (\mathbf{k} + \mathbf{g} + \mathbf{s}_{\mathbf{g}}) \cdot \mathbf{s}_{\mathbf{g}}^{(\mathbf{R})} \Phi_{\mathbf{g}} - \pi i \sum_{\mathbf{g}'} (1 - \delta_{\mathbf{g}\mathbf{g}'}) \frac{U_{\mathbf{g}-\mathbf{g}'}}{\beta_{\mathbf{g}}} \Phi_{\mathbf{g}'}. \quad (13)$$

The second term in the right-hand side of (12) in the limit of small width W of a cell is given by

$$\lim_{\Delta z \rightarrow 0} \lim_{W \rightarrow 0} \frac{1}{\Delta z} \left\{ \left(\frac{\Delta z}{W} \tan \theta_{g'} \right) \left[\Phi_{g'}^{(out)}(\nu, z + \Delta z) - \Phi_{g'}^{(out)}(\nu - 1, z + \Delta z) \right] \right\} = \tan \theta_{g'} \frac{\partial \Phi_{g'}(x, z)}{\partial x},$$

and hence the combined effect of propagation through a slice *and* the subsequent application of the interpolation formulae is equivalent to a differential equation

$$\frac{\partial \Phi_{\mathbf{g}}(x, z)}{\partial z} + \tan \theta_{\mathbf{g}} \frac{\partial \Phi_{\mathbf{g}}(x, z)}{\partial x} = \frac{2\pi i}{\beta_{\mathbf{g}}} (\mathbf{k} + \mathbf{g} + \mathbf{s}_{\mathbf{g}}) \cdot \mathbf{s}_{\mathbf{g}}^{(\mathbf{R})} \Phi_{\mathbf{g}} - \pi i \sum_{\mathbf{g}'} (1 - \delta_{\mathbf{g}\mathbf{g}'}) \frac{U_{\mathbf{g}-\mathbf{g}'}}{\beta_{\mathbf{g}}} \Phi_{\mathbf{g}'}. \quad (14)$$

Taking into account the fact that $\tan \theta_{\mathbf{g}} = (\mathbf{k} + \mathbf{g})_x / (\mathbf{k} + \mathbf{g} + \mathbf{s}_{\mathbf{g}})_z$ and that $\beta_{\mathbf{g}} = (\mathbf{k} + \mathbf{g} + \mathbf{s}_{\mathbf{g}})_z$ we see that the equation set (14) is equivalent to the Howie-Basinski equations.